Nano Research

Open Access

Research Article

Self-standing 3D magnetoplasmonic nanostructures with enhanced Faraday effect and outstanding sensing performance

Shixin Sun[1], Tong-Huai Cheng[2] ✉, Xiang Gao[3], Junfeng Liu[3], Muhan Tang[1], Xiaolei Sun[3] ✉, and Feng Luo[1,3] ✉

[1] College of Electronic Information and Optical Engineering, Nankai University, Tianjin 300350, China
[2] Department of Electronic and Information Engineering, School of Engineering, Westlake University, Hangzhou 310030, China
[3] Tianjin Key Lab for Rare Earth Materials and Applications, Center for Rare Earth and Inorganic Functional Materials, School of Materials Science and Engineering, Nankai University, Tianjin 300350, China

Cite this article: *Nano Research*, **2026**, *19*, 94908446. https://doi.org/10.26599/NR.2026.94908446

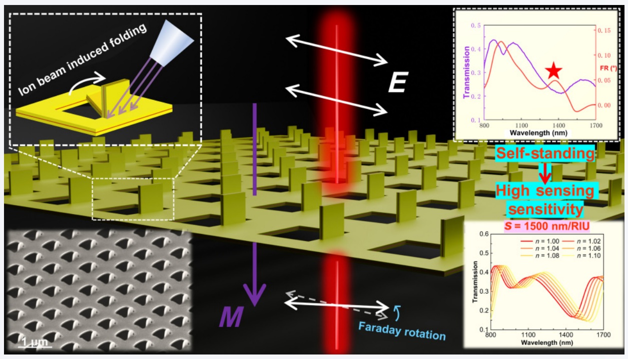

ABSTRACT: Engineered magnetoplasmonic nanostructures offer an efficient route to enhance the magneto-optical (MO) activity of materials, greatly improving their practical utility. Especially, three-dimensional (3D) magnetoplasmonic nanostructures offer richer MO properties through multi-mode excitations, providing new paradigms for miniaturized non-reciprocal photonic devices. However, the complex geometrical configurations of 3D nanostructures impose significant fabrication challenges compared to conventional planar nanostructures, which creates substantial obstacles for practical implementation. Here, we present free-standing metallic hole-vertical nanoplate (MH-VNP) nanostructures fabricated by high-precision focused ion beam (FIB) technology on Au/Co/Au trilayers. Under *y*-polarized excitation, MH-VNPs exhibit an unusual Fano resonance arising from in-phase conductive coupling between the nanoplate and metallic hole, thereby forming 3D currents. This resonance induces strong magnetic field localization, causing a larger Faraday rotation (FR) and enabling FR sign inversion. Systematic modulation of geometric parameters allows precise control of FR magnitude and resonance positions, offering versatile tunability. The self-supported architecture maximizes exposure to the surrounding medium, achieving an exceptional refractive index sensitivity of up to 1500 nm/RIU (RIU = refractive index unit). Overall, this work demonstrates an environmentally friendly fabrication route for 3D magnetoplasmonic structures, offering a versatile approach for tailoring MO responses in nonreciprocal photonic and sensing applications.

KEYWORDS: Faraday rotation, Fano resonance, three-dimensional (3D) nanostructure, free-standing, sensing

1 Introduction

The magneto-optical (MO) effect is a physical phenomenon wherein magnetic materials exhibit optical anisotropy under an applied external magnetic field. This effect manifests as dynamic modulation of the polarization state (e.g., Faraday effect or Kerr effect) or nonreciprocal transmission of incident light, which plays a critical role in conventional optical isolators [1, 2], circulators [3, 4], and optical communication systems [5], and has even enabled omnidirectional nonreciprocal absorption in MO hypercrystals [6]. In broader studies of nonreciprocal transport, non-Hermitian anti-parity-time (PT)-symmetric circuits exploiting level pinning have also been demonstrated to realize robust and self-adaptive energy transmission [7], highlighting engineered coupling in non-Hermitian platforms as an effective route to nonreciprocal transmission. However, natural MO materials suffer from intrinsically weak responses at optical frequencies and bulky dimensions, severely limiting their integration into compact and efficient photonic devices. Artificial design and fabrication of tailored micro-nano structures offer a powerful approach to substantially enhance the intrinsic MO properties of materials [8]. Consequently, MO metamaterials and metasurfaces have garnered significant attention over the past decade [9–17]. Undoubtedly, leveraging the highly localized interfacial electromagnetic field generated by surface plasmon resonance (SPR) in metallic nanostructures to enhance the MO effect stands out as one of the

Received: October 13, 2025; **Revised:** December 2, 2025
Accepted: January 13, 2026

✉ Address correspondence to Tong-Huai Cheng, chengtonghuai@westlake.edu.cn; Xiaolei Sun, xiaolei.sun@nankai.edu.cn; Feng Luo, feng.luo@nankai.edu.cn

most effective strategies [18–22]. This has subsequently given rise to the interdisciplinary field of magnetoplasmonics [23–25]. On the other hand, ferromagnetic metals exhibit high optical losses within the visible spectrum, resulting in a broad full width at half maximum (FWHM) for plasmonic resonance peaks, constraining their applicability in sensing field. To address this, researchers pursued the construction of heterostructures combining ferromagnetic metals (e.g., Fe and Co) with noble metals (e.g., Au and Ag) [26–28]. This strategy leverages the superior MO properties of the former and the exceptional plasmonic characteristics of the latter to optimize the overall MO figure of merit (FOM) of the device. Within this framework of metallic heterostructure systems, researchers explored various nanostructures, including nanodisks [29, 30], nanorings [31, 32], nanoholes [33], split-rings [34], and chiral geometries [35, 36]. Furthermore, the introduction of Fano resonances was demonstrated as an effective approach for enhancing the magneto-optical Kerr effect (MOKE) and achieving sign reversal [37, 38]. These findings demonstrate that Fano resonance in ingeniously designed MO nanostructures enables effective modulation of both the intensity and phase in MO effects, thereby significantly improving their sensing sensitivity.

Despite significant advancements in magnetoplasmonic metasurfaces, numerous challenges remain to be addressed. For example, conventional planar nanostructures exhibit limited resonant modes and possess low degrees of freedom for optical manipulation. Consequently, three-dimensioanl (3D) nanostructures with out-of-plane asymmetry have attracted considerable research interest in recent years [39–42]. Compared to their planar counterparts, 3D nanostructures provide stronger optical responses and introduce groundbreaking degrees of freedom for photonic device engineering. However, reports on 3D MO nanostructures remain notably scarce to date. Harnessing optical resonant modes in 3D nanostructures to efficiently manipulate MO effects would significantly advance the development of novel MO devices. Nevertheless, the fabrication of 3D nanostructures operational at optical frequencies presents extreme challenges. Furthermore, unlike non-magnetic materials such as silicon or titanium dioxide, magnetic thin films exhibit low volatility that renders conventional etching techniques (e.g., inductively coupled plasma (ICP) and reactive ion etching (RIE)) ineffective. Another critical concern involves the safety of nanofabrication methodologies. Traditional lithographic processes utilize substantial organic compounds (e.g., photoresists, developers, and acetone), posing serious environmental contamination risks and potential health hazards. Therefore, developing effective and environmentally benign fabrication processes will establish a crucial foundation for practical applications of 3D magnetoplasmonic nanostructures.

Herein, we propose the self-standing 3D MO nanostructures, metal hole-vertical nanoplate (MH-VNP) arrays, manufactured by a cleaner nanofabrication process utilizing a water-soluble sacrificial layer and focused ion beam (FIB) technology. In contrast to conventional lithographic processes, the presented methodology demonstrates enhanced simplicity and remains entirely free from environmentally hazardous organic compounds throughout all fabrication stages. The transmission spectra and Faraday rotation (FR) values of the 3D nanostructures were characterized using a custom-built optical system, and two resonant dips at 950 and 1430 nm wavelengths were observed under a normal *y*-polarized incidence. The numerical results from COMSOL Multiphysics demonstrate that the 3D nanostructures exhibit an unusual Fano resonance, attributed to the formation of 3D coupled currents at the junctions between MH and VNP. The resonance significantly enhances the localized magnetic field intensity, consequently giving rise to the FR peak. The impacts of structural variables (including Au film thickness, nanoplate height, and array periodicity) on transmission and FR spectra were investigated both in experiments and simulations. These geometric modifications induce systematic spectral shifts in the transmission and FR curves, accompanied by the changes in FR intensity, enabling flexible tuning of the MO behaviors. Furthermore, owing to the free-standing configuration, the nanostructure exhibits exceptional sensitivity to ambient refractive index variations, with a high sensing sensitivity of 1500 nm/RIU (RIU = refractive index unit). Our fundings offer a promising pathway to develop ultrasensitive MO nonreciprocal devices.

2 Experimental

2.1 Sample fabrication

A $Sr_3Al_2O_6$ sacrificial layer (~ 40 nm thick) was deposited on a $SrTiO_3$ substrate (5 mm × 5 mm × 1 mm) via pulsed laser deposition (PLD). Subsequently, an Au/Co/Au trilayer with a total thickness of 40 nm (comprising two 14 nm thick Au outer layers sandwiching a 12 nm thick Co interlayer) was sputtered onto the sacrificial layer by magnetron sputtering. The multilayer sample was then immersed in deionized water at room temperature. After several hours, complete dissolution of the $Sr_3Al_2O_6$ layer released the Au/Co/Au film, which remained suspended on the water surface. This free-standing film was retrieved using a copper mesh and air-dried in a clean environment sufficiently. During drying, capillary forces induced spontaneous flattening of the Au/Co/Au film, forming a smooth and substrate-free membrane, as schematically illustrated in Fig. 1(a). This fabrication route eliminated environmentally unfriendly organic compounds common to conventional nanofabrication, which was a critical advantage for sustainable nanofabrication.

Then the self-standing film was transferred to a FIB microscope (Helios 5 CX) for structuring. Initially, the 2D nanoplate pattern was outlined by ion beam milling (Ga^+, 30 kV, and 40 pA) on the Au/Co/Au film. Precise ion bombardment at the bottom of the nanoplate with optimized dose then induced gradual nanoplate tilting, ultimately making it perpendicular to the MH plane (Fig. 1(b)). This process enabled the transformation of the structure from two-dimensioanl (2D) to 3D. Figure 1(c) presents the morphology of the MH-VNP array. In our experiments, the MH-VNP structures showed good mechanical stability under ambient laboratory conditions. The nanoplates remained upright and intact over time; the bending, collapse, or degradation of the vertical nanoplates were not observed, even when samples were exposed to air and gentle handling.

2.2 Transmission spectra and FR characterization

The transmission spectra and FR of the MH-VNP arrays were characterized using a custom-built optical measurement system (Fig. 1(d)). In all measurements, linearly polarized light with either *x*- or *y*-polarization was incident normal to the sample surface (i.e., propagating along the *z*-axis). For transmission measurements, the

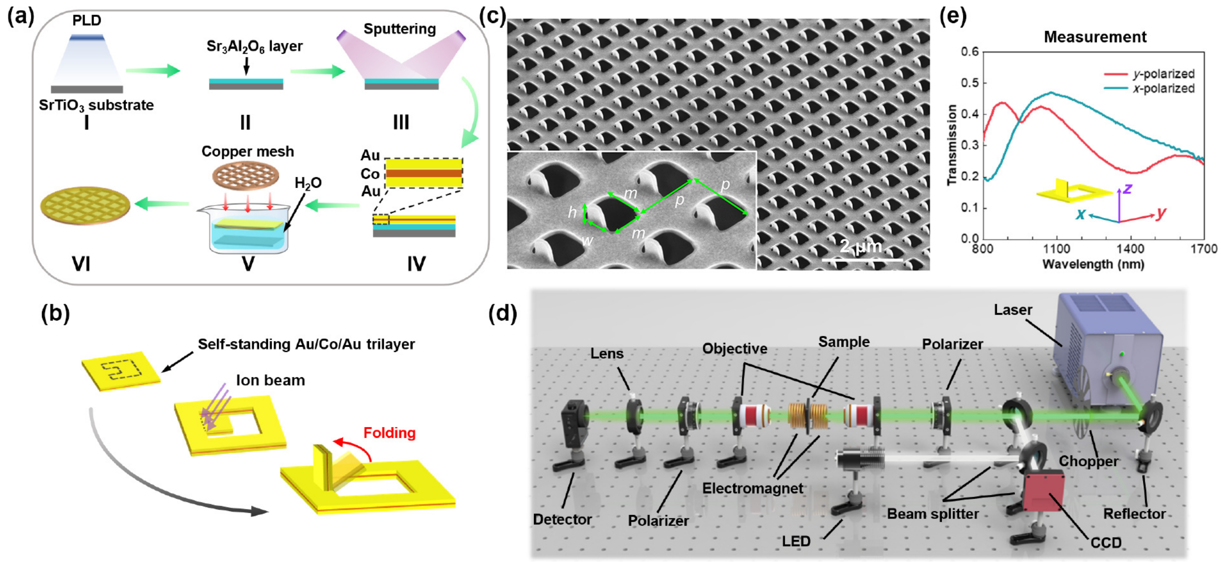

Figure 1 (a) Preparation process of the substrate-free Au/Co/Au film. (b) Processing of the MH-VNP structure using FIB. The nanoplate was gradually perpendicular to the MH plane during constant bombardment of the bottom of the nanoplate with ion beam. (c) Scanning electron microscopy (SEM) images of the MH-VNP array, with the geometrical dimensions of p = 700 nm, m = 400 nm, w = 200 nm, and h = 200 nm. (d) Custom-built optical characterization system. (e) Measured transmission spectra of the MH-VNP arrays under x- and y-polarized incidence.

incident polarization was controlled via a front polarizer, while the electromagnet and rear polarizer were removed, and the transmitted signals normalized against air yielded the transmission spectra under x- and y-polarized illumination. For FR measurements, the sample was vertically mounted between the pole boots of an electromagnet, and a magnetic field up to 0.5 T was applied along the z-axis (Faraday geometry). In this configuration, a rear polarizer was positioned nominally orthogonal to the front polarizer, and the FR angles were calculated from the corresponding transmittance measurements.

2.3 Simulation

Numerical simulations were performed using the finite element method implemented in COMSOL Multiphysics. Periodic boundary conditions were applied along both the x and y directions to model an infinite array. In the z direction, perfectly matched layers (PMLs) were added to both the top and bottom boundaries to suppress artificial reflections. The MO activity of the Co layer under external magnetic field was introduced by modifying the off-diagonal components of its relative permittivity tensor.

3 Results and discussion

As 3D nanostructures possess richer optical properties than their 2D counterparts, the transition from 2D to 3D nanostructures deserves particular attention in this stage. The VNP patterns were formed via ion-beam-induced folding, achieved by bombarding their basal regions. Throughout this process, the folding angle can be precisely regulated through meticulous control of the ion dose. As illustrated in Fig. S1 in the Electronic Supplementary Material (ESM), the nanoplate gradually transitions to a vertical orientation under continuous ion irradiation, with a positive correlation between ion dose and folding angle, until VNP perpendicular to the MH plane is attained, and the geometric parameters are defined as p = 700 nm, m = 400 nm, h = 200 nm, and w = 200 nm. The transmission spectra (under normal incidence along the z-axis) of the self-standing 3D nanostructures were characterized utilizing a self-constructed optical characterization system (Fig. 1(d)), and the measured results are shown in Fig. 1(e). When the incident light is x-polarized (i.e., polarization direction parallel to the VNP plane), the transmission spectrum exhibits no resonance dips. On the contrary, y-polarized excitation (polarization direction perpendicular to the VNP plane) generates two pronounced resonance dips at approximately 950 and 1430 nm wavelengths, which are absent in planar plate counterparts [34].

To elucidate the resonance mechanisms of the MH-VNP array, its transmission spectra were simulated under x- and y-polarized incidence. As shown in Fig. 2(a), the x-polarization transmission spectrum reveals no resonant features, and the y-polarization transmission spectrum exhibits two distinct dips at 960 (low-wavelength dip (LWD)) and 1450 nm (high-wavelength dip (HWD)). These computational results corroborate the experimental measurements presented in Fig. 1(e), confirming the reliability of our custom optical measurement system. The minor spectral differences between simulation and experiment are attributed to fabrication variations from the FIB process.

Subsequently, near-field distributions at the LWD and HWD wavelengths were computed, with local current directions marked by green arrows in Figs. 2(c)–2(h). Cross-sectional of x–z plane simulations reveal oscillating currents along the MH periphery and VNP sidewalls. At the LWD (Figs. 2(c) and 2(e)), anti-phase current oscillations inhibit closed-loop formation at the junction of MH and VNP, indicating an anti-symmetric coupling mode [43]. This manifests as locally enhanced electric fields at the VNP apex and intensified magnetic fields at its lateral surfaces. Conversely, at the HWD (Figs. 2(d) and 2(f)), in-phase currents establish localized closed loops, characteristic of a symmetric coupling mode. This configuration generates electric field enhancement at the VNP apex and magnetic field concentration in the joint of MH and VNP. Figures 2(g) and 2(h) present magnetic field distributions in the x–y plane, revealing pronounced confinement at both MH corners and VNP vicinity for LWD, whereas HWD exhibits primary magnetic localization near the VNP. This difference arises because in-phase coupling induces localized circulating currents, which generate

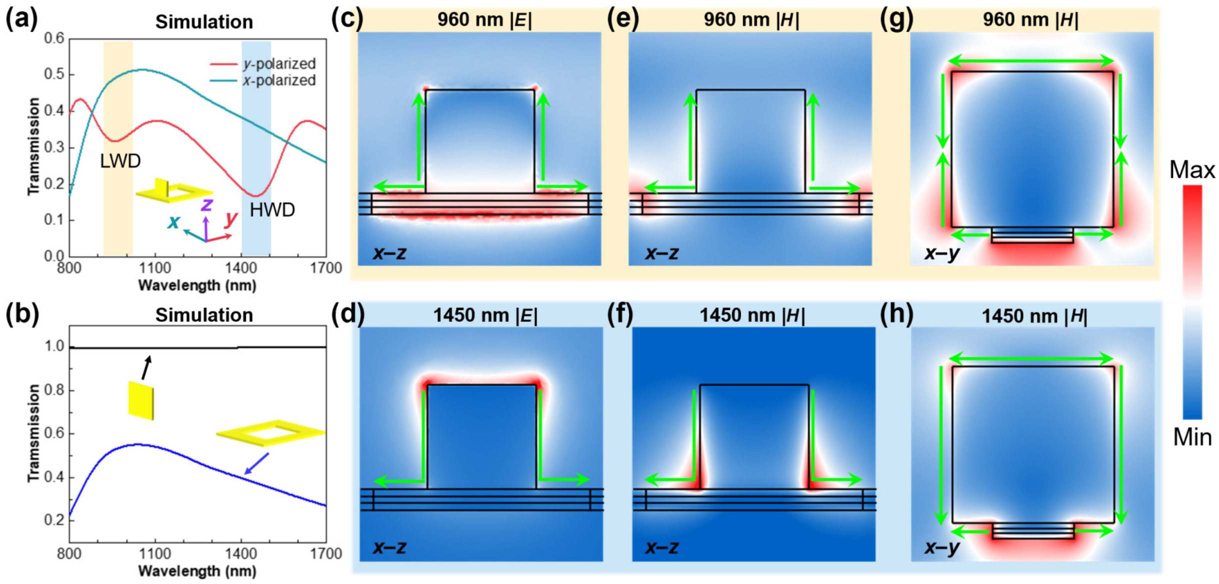

Figure 2 (a) Simulated transmission spectra of the MH-VNP array with the above-mentioned geometric dimensions under *x*- and *y*-polarized incidence. (b) Simulated transmission spectra of the planar MH array and detached VNP array with the same dimensions as above under *y*-polarized normal incidence. (c) Electric field and (e) magnetic field distributions at the *x*–*z* cross-section at 960 nm wavelength under *y*-polarized normal incidence, in which green arrows indicate the direction of local current, and the same below. (d) Electric field and (f) magnetic field distributions at the *x*–*z* cross-section at 1450 nm wavelength under *y*-polarized normal incidence. (g) Magnetic field distribution at the *x*–*y* cross-section at 960 nm wavelength under *y*-polarized normal incidence. (h) Magnetic field distribution at the *x*–*y* cross-section at 1450 nm wavelength under *y*-polarized normal incidence.

magnetic field enhancements confined to structural corners, whereas anti-phase coupling cannot.

To understand the resonance origins, the MH-VNP array was deconstructed into a planar MH array and VNPs were isolated, then their individual spectra were simulated (Fig. 2(b)). The planar MH array exhibits a broad and gently sloped feature (blue curve), signifying extraordinary optical transmission (EOT) resulting from periodicity-induced SPR and localized plasmonic waveguide modes [44]. This phenomenon was further corroborated by our experimental measurements (Fig. S2 in ESM). In contrast, the isolated VNPs spectrum (black curve in Fig. 2(b)) remains spectrally flat, attributable to its limited thickness of merely 40 nm along the *y*-direction, which precludes pronounced resonances within the near-infrared regime. Additionally, electromagnetic field distribution simulations were performed on the 2D counterpart of the MH-VNP, as illustrated in Fig. S3 in the ESM. Figure S3(a) in the ESM presents the transmission spectra of the MH-VNP and its 2D counterpart under *y*-polarized normal incidence, while Figs. S3(b) and S3(c) in the ESM depict their schematic structures. Figures S3(d)–S3(i) in the ESM display the electromagnetic field distributions of the 2D counterpart at its resonant wavelength. It is evident that the MH-VNP exhibits stronger resonance intensity and superior field localization capability compared to its 2D counterpart. Consequently, the resonant dip observed in the transmission spectrum of the MH-VNP array can be attributed to the coupling effect between planar MH array and VNPs. As widely recognized, Fano resonance formation requires synergistic interaction between two distinct entities: a broadband continuum state and a narrowband discrete state. Within the nanostructure of our work, the MH element functions as the continuum counterpart, providing a broad spectral background via EOT. Meanwhile, symmetry constraints dictate that only currents parallel to the incident polarization direction can radiate into the far-field, and the *z*-propagating currents along VNP sidewalls remain non-radiative (constituting a dark mode) as they are neither directly excitable by incident light nor capable of far-field emission. This dark mode thus represents the discrete state. The efficient coupling between these components establishes a 3D conductive interaction, thereby generating the observed Fano resonance in MH-VNP transmission spectra [43].

Based on the preceding analysis, the influence of the Fano resonance on the MO effect was investigated subsequently. The transmission (Fig. 3(b)) and FR spectra (Fig. 3(c)) of MH-VNP structures with varying Au layers thickness (Fig. 3(a)) were measured using our self-built MO characterization system. The experimental results were corroborated by corresponding numerical simulations (Figs. 3(d) and 3(e)), which show good agreement with the measured data. The FR values were computed according to the following expression

$$\mathrm{FR} = \mathrm{Re}\left(\arctan\left(\frac{T_x}{T_y}\right)\right) \tag{1}$$

where T_x and T_y represent the transmitted intensity components along the *x*- and *y*-directions, respectively (under *y*-polarized illumination). This formulation reveals two distinct pathways for enhancing MO effect. First, enhancing T_x by increasing the MO contribution, which can be achieved by using thicker ferromagnetic layers or materials with higher permeability [23]. Second, leveraging the pure optical effect by reducing T_y, as seen in the resonance dip at Fano resonance wavelengths. Within the quantum electrodynamic framework, the microscopic origin of MO effects resides in spin-orbit coupling mediated interactions between incident electromagnetic fields and electron spins [45]. The corresponding Hamiltonian takes the form

$$H_{\mathrm{int}} = -\mu_{\mathrm{s}} \cdot B_{\mathrm{eff}} \tag{2}$$

where μ_{s} denotes the electron spin magnetic moment and B_{eff} represents the effective magnetic field induced by the optical electric

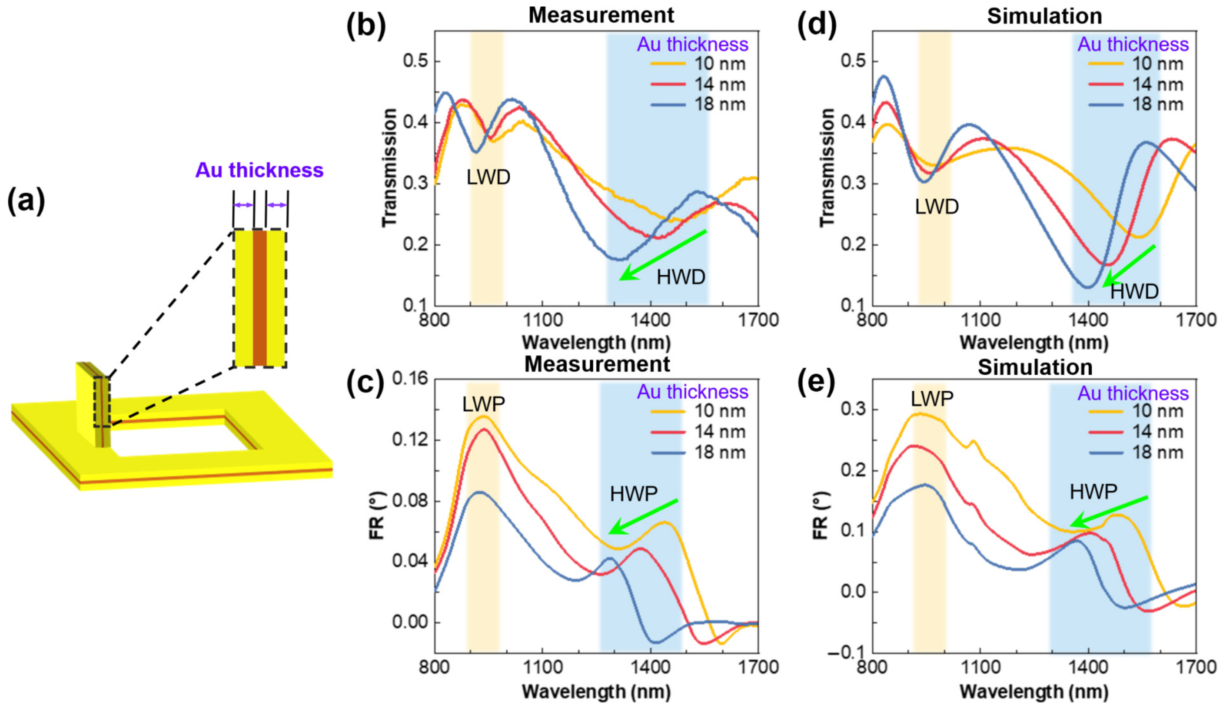

Figure 3 (a) Schematic illustration of varied Au layer thickness. (b) Measured and (d) simulated transmission spectra of the MH-VNP structures with different Au layer thicknesses under *y*-polarized incidence. (c) Measured and (e) simulated FR curves of the MH-VNP structures with different Au layer thicknesses under *y*-polarized incidence.

field. The electron spin state is modulated by intrinsic local electromagnetic fields within the material (e.g., encompassing crystal fields, exchange fields, and external fields) manifesting as Zeeman splitting or spin precession dynamics [45, 46]. Consequently, tailoring the distribution of local electromagnetic fields (intensity, gradient, or modal symmetry) could enables active enhancement of MO effects such as FR and Kerr angle, with quantitative relationships governed by the off-diagonal components of the MO dielectric tensor.

As evidenced in Figs. 3(c) and 3(e), all spectra exhibit FR enhancement peaks in the vicinity of 950 nm (low wavelength peak (LWP)). This anticipated behavior originates from local electromagnetic field amplification by the MH array, where the planar MH array demonstrates analogous FR enhancement near 950 nm, and this assertion is further corroborated by Fig. S4 in ESM. Meanwhile, the HWD induced by SPR generates a corresponding high wavelength peak (HWP) in the FR spectra, manifesting at 1380, 1400, and 1490 nm for Au thicknesses of 10, 14, and 18 nm, respectively (Fig. 3(c)). This result is consistent with the result obtained from the simulation (Fig. 3(e)). Notably, the planar MH array and detached VNPs individually show no FR enhancement in these ranges. However, upon assembly into MH-VNP configurations, the Fano resonance-mediated field amplification gives rise to pronounced HWP features. Additionally, the null point of FR emerges within the spectral bandwidth of the Fano resonance. This phenomenon stems from the abrupt phase shift inherent in the forced damped harmonic oscillator model: As the incident photon energy approaches the plasmon resonance frequency, the phase of electron oscillations undergoes an abrupt shift, reversing the direction of the Lorentz force [38]. Consequently, this reversal transfers angular momentum to the incident light, thereby inverting its helicity.

In addition to the unusual Fano resonance achieved by the 3D MH-VNP structure for FR enhancement, the systematic spectral variations induced by altering the Au layer thickness were also observed. Increasing the Au layer thickness induces a blue shift in both the transmission resonance dip and FR peak, accompanied by reduced transmittance at the dip and diminished FR magnitude at the peak (Fig. 3). This behavior arises because thicker Au weakens localized surface plasmon excitation within the MH array, particularly reducing the vertical electric field component. Therefore, the excitation efficiency of the dark mode in the Fano resonance decreases, lowering coupling efficiency and elevating resonance energy (blue shift). The attenuated vertical field also suppresses spin-orbit coupling efficiency, diminishing the FR peak intensity. Simultaneously, increased Ohmic losses dissipate more optical energy, further reducing transmittance at the spectral dip. Correspondingly, the effects of varying Co thickness on the transmission spectra and FR curves of the MH-VNP were also simulated, as shown in Figs. S5(a)–S5(c) in the ESM. In summary, increasing the Co thickness leads to a slightly broader transmission resonance dip and a higher Faraday rotation magnitude. Physically, a thicker Co layer increases the MO path length, thereby enhancing the FR. At the same time, we find that the HWP of FR curves becomes more flattened when Co is thicker. This occurs because the added Co thickness introduces greater optical loss as Co is a lossy ferromagnetic metal, which tends to damp and broaden the resonance-driven features.

In the following, MH-VNP arrays with varying VNP heights (Figs. 4(a)–4(c)) and periods (Figs. 5(a)–5(c)) were fabricated, and their transmission spectra and FR were characterized. These experimental results were further corroborated by numerical simulations. Figures 4(d)–4(g) clearly shows that increasing VNP height induces a red shift in both the transmission dip and FR enhancement peak, with reduced transmittance at the dip and increased FR at the peak. The spectral red shift arises from the

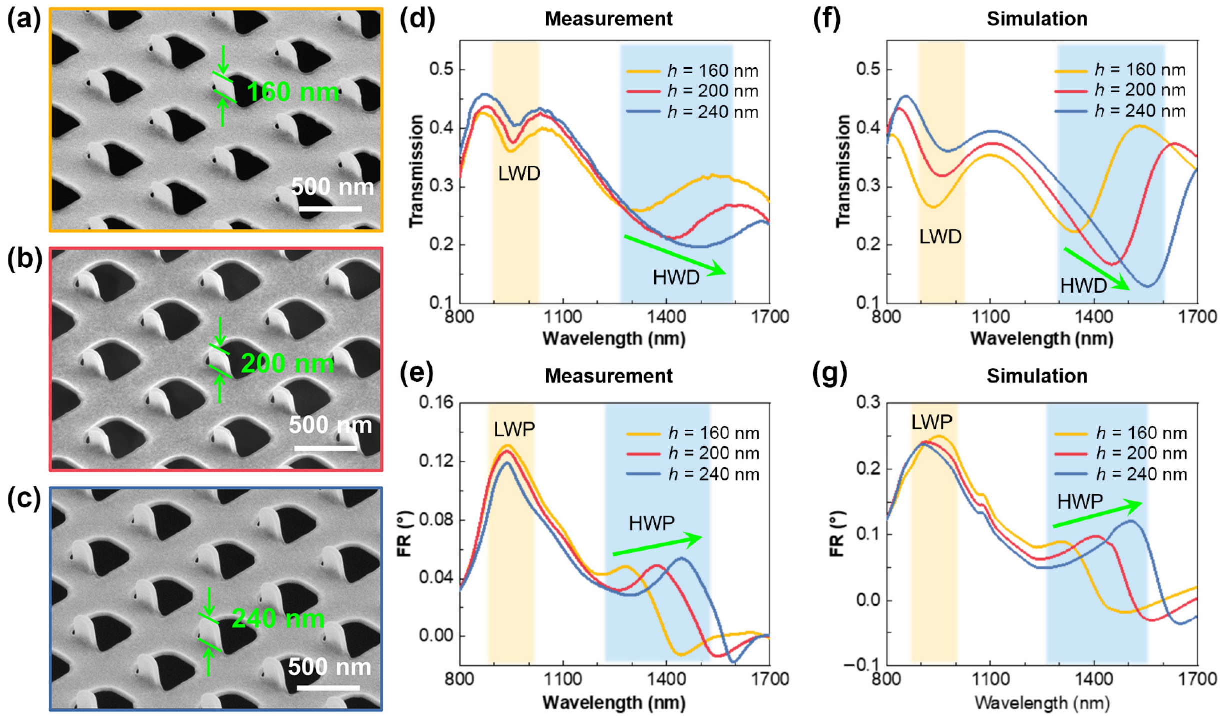

Figure 4 (a)–(c) SEM images of the MH-VNP arrays with different VNP heights (160, 200, and 240 nm, respectively). (d) Measured and (f) simulated transmission spectra of the MH-VNP arrays with different VNP heights under *y*-polarized incidence. (e) Measured and (g) simulated FR curves of the MH-VNP arrays with different VNP heights under *y*-polarized incidence.

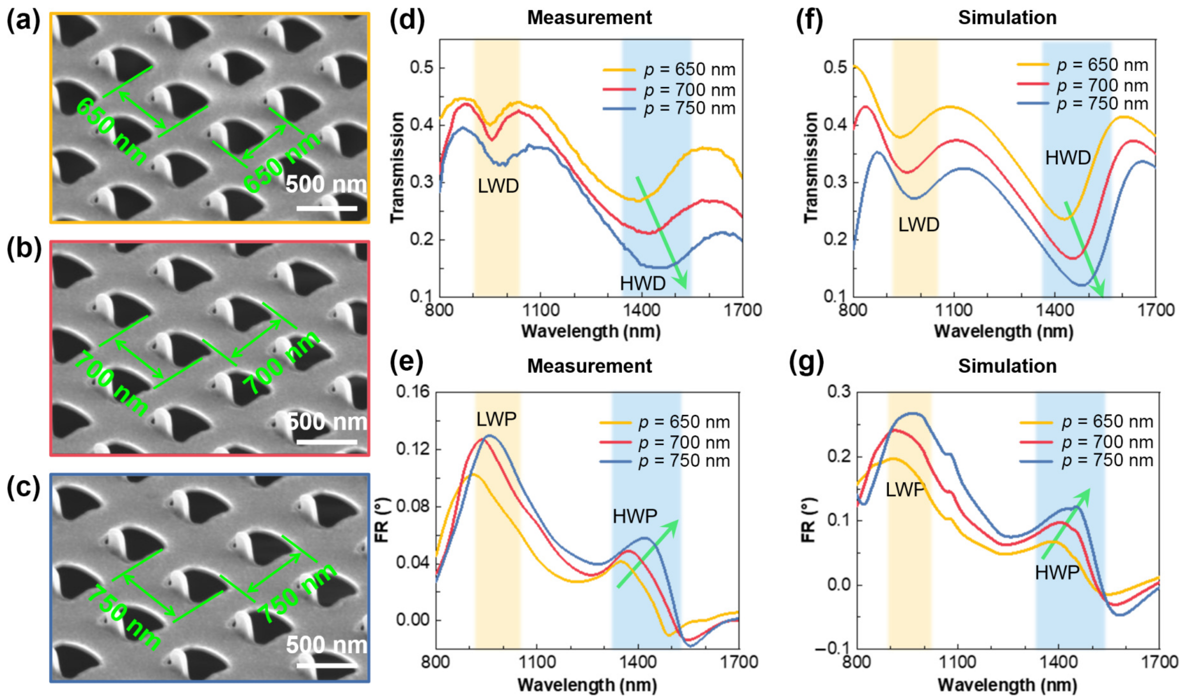

Figure 5 (a)–(c) SEM images of the MH-VNP arrays with different periods (650, 700, and 750 nm, respectively). (d) Measured and (f) simulated transmission spectra of the MH-VNP arrays with different periods under *y*-polarized incidence. (e) Measured and (g) simulated FR curves of the MH-VNP arrays with different periods under *y*-polarized incidence.

lengthened 3D current path, consistent with prior reports [43]. This height increase simultaneously augments optical losses, further reducing transmittance. Additionally, the enhanced localized magnetic field elevates the FR resonance amplitude.

On the other hand, increasing the array period red-shifts both the Fano resonance dip and FR enhancement peak (Figs. 5(d)–5(g)), as this directly scales the SPR wavelength proportionally. Concurrently, reduced unit density (i.e., larger array period) lowers overall transmittance, meanwhile, it weakens inter-element optical coupling, reducing radiative damping of resonance. This preserves the intrinsic high-quality factor of individual units, and the enhanced electromagnetic field confinement within each unit further amplifies the FR peak magnitude. Notably, structural parameter variations differentially impact the two resonance dips (LWD and HWD) and FR peaks (LWP and HWP). LWD and LWP exhibit greater stability against parameter changes. This robustness stems from the anti-phase current coupling between MH and VNP units at these wavelengths (Figs. 2(c) and 2(e)), resulting in relative independence and diminished sensitivity. Collectively, these results offer new possibilities for tailoring device performance through structural engineering.

Furthermore, the free-standing configuration of the sample enables the device to interact fully with the surrounding medium, thereby effectively enhancing its sensing sensitivity. To investigate this, the refractive index sensing performance of the structure was numerically simulated under y-polarized incidence, with the results presented in Fig. 6. As the environmental refractive index gradually increases from 1.0 to 1.1, both resonance dips in the transmission spectrum and the FR resonance peak exhibit a distinct red shift. To quantitatively determine the sensing sensitivity, the resonance positions of the HWD of the transmission spectrum and the HWP of the FR curve are plotted as linear functions of the refractive index in Figs. 6(c) and 6(d), respectively. The slopes of the linear fits represent the corresponding sensing sensitivities. As anticipated, the free-standing MH-VNP structure achieves a remarkable sensing sensitivity up to 1500 nm/RIU. Meanwhile, the sensing sensitivities of the MH-VNP both in reflection spectra and transverse magneto-optical Kerr effect (TMOKE) are presented in Figs. S6(a)–S6(d) in the ESM. The sensing sensitivity reaches up to 1200 nm/RIU in both cases. All these results demonstrate that the performance of our fabricated nanostructure in refractive index sensing is outstanding compared to previously reported devices [47–50] (further details can be found in Table S1 in the ESM), providing a novel strategy for developing highly sensitive magneto-optical sensors.

4 Conclusions

In summary, we report a green and efficient technology for the construction of the 3D MH-VNP nanostructures with enhanced FR and excellent sensing characteristics. Crucially, the entire fabrication process eliminates environmentally hazardous substances, establishing an environmentally benign nanofabrication route distinct from conventional lithography-based approaches. Under y-polarized incident light, the MH-VNP arrays excite an unusual Fano resonance through 3D conductive coupling, which is unobserved in isolated MH or detached VNP. The Fano resonance enhances localized electromagnetic fields, simultaneously amplifying FR magnitude and inducing sign reversal. Leveraging the nanoscale precision of FIB technology, the optical and MO responses affected by the minor variations in structural dimensions were systematically investigated, enabling the tunable MO activity in wide wavelength ranges. Furthermore, the free-standing configuration permits full environmental exposure, yielding an exceptional refractive index sensitivity (1500 nm/RIU). Clearly, our work establishes a new paradigm for enhancing and tuning FR, with prominent application potential for MO sensing and isolation.

Electronic Supplementary Material: Supplementary material (Figs. S1–S6 and Table S1) is available in the online version of this article at https://doi.org/10.26599/NR.2026.94908446.

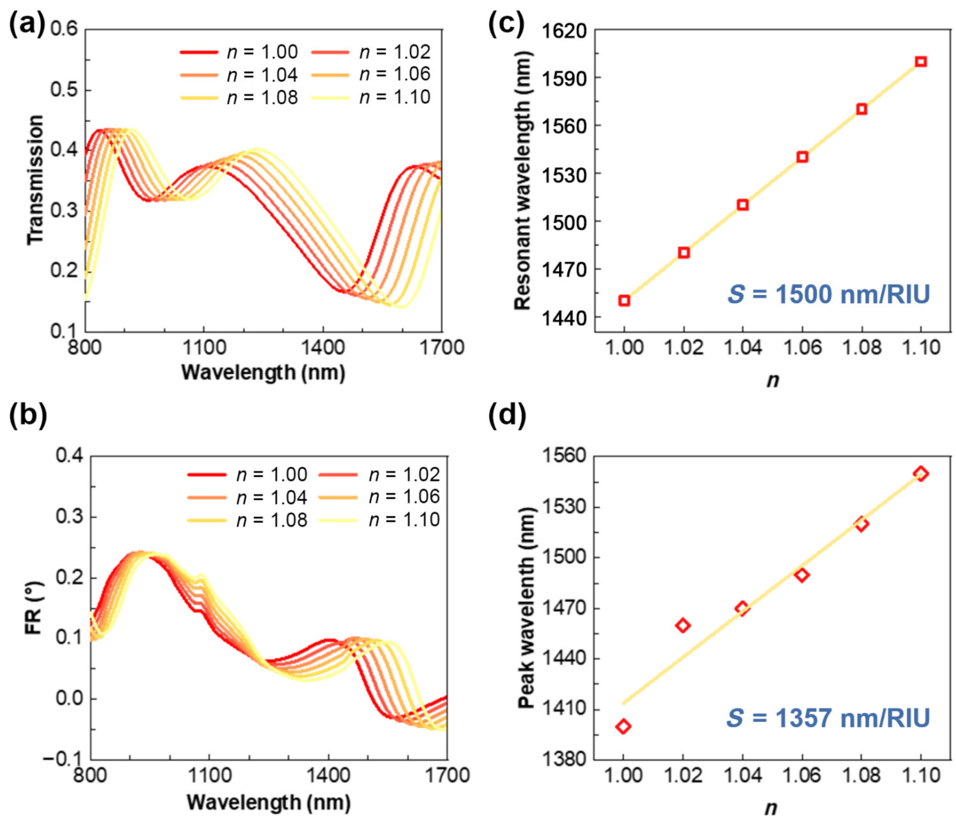

Figure 6 Optical and MO sensing performances of the MH-VNP nanostructure. Effects of various refractive index on (a) the transmission and (b) FR spectra of the MH-VNP nanostructure under y-polarized incidence. The linear dependence of the resonant positions of (c) HWD in the transmission spectra, and (d) HWP in the FR curves on the refractive index. The slopes of the linear fits, indicated by the blue text, represent the optical and MO sensing sensitivities, respectively.

Data availability

All data needed to support the conclusions in the paper are presented in the manuscript and the Electronic Supplementary Material. Additional data related to this paper may be requested from the corresponding author upon request.

Acknowledgements

This work was supported by the National Key Research and Development Program of China (No. 2021YFA1601004).

Declaration of competing interest

All the contributing authors report no conflict of interests in this work.

Author contribution statement

S. X. S. and T.-H. C. designed and carried out the experiments, analyzed data, and wrote the draft. X. G. and J. F. L. helped with custom-built optical measurement system. M. H. T performed the sample fabrication. X. L. S. participated in the discussion and revision of the draft. F. L. provided resources, directed research efforts, and reviewed and revised the manuscript. All the authors have approved the final manuscript.

Use of AI statement

None.

References

[1] Jalas, D.; Petrov, A.; Eich, M.; Freude, W.; Fan, S. H.; Yu, Z. F.; Baets, R.; Popović, M.; Melloni, A.; Joannopoulos, J. D. et al. What is—and what is not—An optical isolator. *Nat. Photonics* **2013**, *7*, 579–582.

[2] Yu, Z. F.; Fan, S. H. Complete optical isolation created by indirect interband photonic transitions. *Nat. Photonics* **2009**, *3*, 91–94.

[3] Yan, W.; Yang, Y. C.; Liu, S. Y.; Zhang, Y.; Xia, S.; Kang, T. T.; Yang, W. H.; Qin, J.; Deng, L. J.; Bi, L. Waveguide-integrated high-performance magneto-optical isolators and circulators on silicon nitride platforms. *Optica* **2020**, *7*, 1555–1562.

[4] Bi, L.; Hu, J. J.; Jiang, P.; Kim, H. S.; Kim, D. H.; Onbasli, M. C.; Dionne, G. F.; Ross, C. A. Magneto-optical thin films for on-chip monolithic integration of non-reciprocal photonic devices. *Materials* **2013**, *6*, 5094–5117.

[5] Qin, J.; Xia, S.; Yang, W. H.; Wang, H. B.; Yan, W.; Yang, Y. C.; Wei, Z. X.; Liu, W. E.; Luo, Y.; Deng, L. J. et al. Nanophotonic devices based on magneto-optical materials: Recent developments and applications. *Nanophotonics* **2022**, *11*, 2639–2659.

[6] Hu, S. Y.; Song, J.; Guo, Z. W.; Jiang, H. T.; Deng, F. S.; Dong, L. J.; Chen, H. Omnidirectional nonreciprocal absorber realized by the magneto-optical hypercrystal. *Opt. Express* **2022**, *30*, 12104–12119.

[7] Guo, Z. W.; Yang, F. Q.; Zhang, H. Y.; Wu, X.; Wu, Q.; Zhu, K. J.; Jiang, J.; Jiang, H. T.; Yang, Y. P.; Li, Y. H. et al. Level pinning of anti-PT-symmetric circuits for efficient wireless power transfer. *Natl. Sci. Rev.* **2024**, *11*, nwad172.

[8] Hadad, Y.; Davoyan, A. R.; Engheta, N.; Steinberg, B. Z. Extreme and quantized magneto-optics with graphene meta-atoms and metasurfaces. *ACS Photonics* **2014**, *1*, 1068–1073.

[9] Xia, S.; Ignatyeva, D. O.; Liu, Q.; Qin, J.; Kang, T. T.; Yang, W. H.; Chen, Y. Q.; Duan, H. G.; Deng, L. J.; Long, D. et al. Enhancement of the Faraday effect and magneto-optical figure of merit in all-dielectric metasurfaces. *ACS Photonics* **2022**, *9*, 1240–1247.

[10] Bi, Y.; Huang, L. L.; Zhao, R. Z.; Zhou, H. Q.; Zhang, W. W.; Zhu, S. Q.; Ullah, N.; Li, X. W.; Wang, Y. T. Magnetically controllable holographic encryption based on a magneto-optical metasurface. *Opt. Express* **2022**, *30*, 8366–8375.

[11] Barsukova, M. G.; Musorin, A. I.; Shorokhov, A. S.; Fedyanin, A. A. Enhanced magneto-optical effects in hybrid Ni-Si metasurfaces. *APL Photonics* **2019**, *4*, 016102.

[12] Cheng, T. H.; Yang, W. H.; Sun, S. X.; Liu, Z. C.; Feng, H. Y.; Qin, J.; Bi, L.; Luo, F. Magnetoplasmonic gratings induced an unusual magneto-optical kerr effect at optical frequencies. *Laser Photonics Rev.* **2025**, *19*, 2401476.

[13] Cheng, T. H.; Yang, W. H.; Liu, Z. C.; Qin, J.; Feng, H. Y.; Li, C. L.; Li, S. C.; Bi, L.; Luo, F. Unconventional transverse magneto-optical kerr effect in cobalt nanopillar arrays. *Adv. Opt. Mater.* **2024**, *12*, 2303242.

[14] Christofi, A.; Kawaguchi, Y.; Alù, A.; Khanikaev, A. B. Giant enhancement of Faraday rotation due to electromagnetically induced transparency in all-dielectric magneto-optical metasurfaces. *Opt. Lett.* **2018**, *43*, 1838–1841.

[15] Máñez-Espina, L. M.; Faniayeu, I.; Asadchy, V.; Díaz-Rubio, A. Extreme nonreciprocity in metasurfaces based on bound states in the continuum. *Adv. Opt. Mater.* **2024**, *12*, 2301455.

[16] Tang, Q.; Zhang, D. D.; Liu, T. T.; Liu, W. X.; Liao, Q. H.; He, J. Z.; Xiao, S. Y.; Yu, T. B. Enhancing Faraday and Kerr rotations based on the toroidal dipole mode in an all-dielectric magneto-optical metasurface. *Opt. Lett.* **2023**, *48*, 3451–3454.

[17] Zhang, X. Q.; Jiang, Y. Q.; Li, Q. Y.; Xu, Y.; Zhan, Q. W.; Zhao, W. S. Giant magneto-optical Kerr effects governed by the quasi-bound states in the continuum. *Opt. Express* **2024**, *32*, 38720–38729.

[18] Bossini, D.; Belotelov, V. I.; Zvezdin, A. K.; Kalish, A. N.; Kimel, A. V. Magnetoplasmonics and femtosecond optomagnetism at the nanoscale. *ACS Photonics* **2016**, *3*, 1385–1400.

[19] Maccaferri, N.; Zubritskaya, I.; Razdolski, I.; Chioar, I. A.; Belotelov, V.; Kapaklis, V.; Oppeneer, P. M.; Dmitriev, A. Nanoscale magnetophotonics. *J. Appl. Phys.* **2020**, *127*, 080903.

[20] Vila, E. F.; Sueiro, X. M. B.; González-Díaz, J. B.; García-Martín, A.; García-Martín, J. M.; Navarro, A. C.; Reig, G. A.; Rodríguez, D. M.; Sandoval, E. M. Surface plasmon resonance effects in the magneto-optical activity of Ag-Co-Ag trilayers. *IEEE Trans. Magn.* **2008**, *44*, 3303–3306.

[21] Bonod, N.; Reinisch, R.; Popov, E.; Nevière, M. Optimization of surface-plasmon-enhanced magneto-optical effects. *J. Opt. Soc. Am. B* **2004**, *21*, 791–797.

[22] Rubio-Roy, M.; Vlasin, O.; Pascu, O.; Caicedo, J. M.; Schmidt, M.; Goñi, A. R.; Tognalli, N. G.; Fainstein, A.; Roig, A.; Herranz, G. Magneto-optical enhancement by plasmon excitations in nanoparticle/metal structures. *Langmuir* **2012**, *28*, 9010–9020.

[23] Armelles, G.; Cebollada, A.; García-Martín, A.; González, M. U. Magnetoplasmonics: Combining magnetic and plasmonic functionalities. *Adv. Opt. Mater.* **2013**, *1*, 10–35.

[24] Wang, L.; Yang, K.; Clavero, C.; Nelson, A. J.; Carroll, K. J.; Carpenter, E. E.; Lukaszew, R. A. Localized surface plasmon resonance enhanced magneto-optical activity in core–shell Fe–Ag nanoparticles. *J. Appl. Phys.* **2010**, *107*, 09B303.

[25] Wang, L.; Clavero, C.; Huba, Z.; Carroll, K. J.; Carpenter, E. E.; Gu, D. F.; Lukaszew, R. A. Plasmonics and enhanced magneto-optics in core–shell Co–Ag nanoparticles. *Nano Lett.* **2011**, *11*, 1237–1240.

[26] Regatos, D.; Fariña, D.; Calle, A.; Cebollada, A.; Sepúlveda, B.; Armelles, G.; Lechuga, L. M. Au/Fe/Au multilayer transducers for magneto-optic surface plasmon resonance sensing. *J. Appl. Phys.* **2010**, *108*, 054502.

[27] Zhu, R. X.; Chen, L. Y.; Zong, Z. X.; Tang, Z. X.; Qian, J.; Tang, S. L.; Du, Y. W. Tuning the shape of magneto-optical Kerr spectrum by changing the strip width in one-dimensional Ag-Co-Ag magnetoplasmonic nanogratings. *Appl. Phys. Lett.* **2019**, *115*, 072405.

[28] Caballero, B.; García-Martín, A.; Cuevas, J. C. Faraday effect in hybrid magneto-plasmonic photonic crystals. *Opt. Express* **2015**, *23*, 22238–22249.
[29] Banthí, J. C.; Meneses-Rodríguez, D.; García, F.; González, M. U.; García-Martín, A.; Cebollada, A.; Armelles, G. High magneto-optical activity and low optical losses in metal-dielectric Au/Co/Au-SiO_2 magnetoplasmonic nanodisks. *Adv. Mater.* **2012**, *24*, OP36–OP41.
[30] de la Osa, R. A.; Saiz, J. M.; Moreno, F.; Vavassori, P.; Berger, A. Transverse magneto-optical effects in nanoscale disks. *Phys. Rev. B* **2012**, *85*, 064414.
[31] Larsson, E. M.; Alegret, J.; Käll, M.; Sutherland, D. S. Sensing characteristics of NIR localized surface plasmon resonances in gold nanorings for application as ultrasensitive biosensors. *Nano Lett.* **2007**, *7*, 1256–1263.
[32] Feng, H. Y.; Luo, F.; Kekesi, R.; Granados, D.; Meneses-Rodríguez, D.; García, J. M.; García-Martín, A.; Armelles, G.; Cebollada, A. Magnetoplasmonic nanorings as novel architectures with tunable magneto-optical activity in wide wavelength ranges. *Adv. Opt. Mater.* **2014**, *2*, 612–617.
[33] Lei, C. X.; Tang, Z. X.; Wang, S. H.; Li, D. Y.; Chen, L. Y.; Tang, S. L.; Du, Y. W. Plasmon resonance enhanced optical transmission and magneto-optical Faraday effects in nanohole arrays blocked by metal antenna. *Opt. Commun.* **2017**, *394*, 41–49.
[34] Cheng, T. H.; Yang, W. H.; Liu, Z. C.; Feng, H. Y.; Qin, J.; Ma, Y. F.; Li, S. C.; Bi, L.; Luo, F. Enhanced Faraday rotation by a Fano resonance in substrate-free three-dimensional magnetoplasmonic structures. *Nanoscale* **2023**, *15*, 15583–15589.
[35] Armelles, G.; Cebollada, A.; Feng, H. Y.; García-Martín, A.; Meneses-Rodríguez, D.; Zhao, J.; Giessen, H. Interaction effects between magnetic and chiral building blocks: A new route for tunable magneto-chiral plasmonic structures. *ACS Photonics* **2015**, *2*, 1272–1277.
[36] Feng, H. Y.; Luo, F.; Arenal, R.; Henrard, L.; García, F.; Armelles, G.; Cebollada, A. Active magnetoplasmonic split-ring/ring nanoantennas. *Nanoscale* **2017**, *9*, 37–44.
[37] Li, L. X.; Zong, X. Y.; Liu, Y. F. Tunable magneto-optical responses in magneto-plasmonic crystals for refractive index sensing. *J. Phys. D: Appl. Phys.* **2020**, *53*, 185106.
[38] Chen, L. Y.; Gao, J. L.; Xia, W. B.; Zhang, S. Y.; Tang, S. L.; Zhang, W. Y.; Li, D. Y.; Wu, X. S.; Du, Y. W. Tunable Fano resonance and magneto-optical response in magnetoplasmonic structure fabricated by pure ferromagnetic metals. *Phys. Rev. B* **2016**, *93*, 214411.
[39] Zhang, X. D.; Liu, Y. L.; Han, J. C.; Kivshar, Y.; Song, Q. H. Chiral emission from resonant metasurfaces. *Science* **2022**, *377*, 1215–1218.
[40] Kilic, U.; Hilfiker, M.; Wimer, S.; Ruder, A.; Schubert, E.; Schubert, M.; Argyropoulos, C. Controlling the broadband enhanced light chirality with L-shaped dielectric metamaterials. *Nat. Commun.* **2024**, *15*, 3757.
[41] Chen, Y.; Deng, H. C.; Sha, X. B.; Chen, W. J.; Wang, R. Z.; Chen, Y. H.; Wu, D.; Chu, J. R.; Kivshar, Y. S.; Xiao, S. M. et al. Observation of intrinsic chiral bound states in the continuum. *Nature* **2023**, *613*, 474–478.
[42] Huo, P. C.; Chen, W.; Zhang, Z. X.; Zhang, Y. Z.; Liu, M. Z.; Lin, P. C.; Zhang, H.; Chen, Z. X.; Lezec, H.; Zhu, W. Q. et al. Observation of spatiotemporal optical vortices enabled by symmetry-breaking slanted nanograting. *Nat. Commun.* **2024**, *15*, 3055.
[43] Liu, Z. G.; Liu, Z.; Li, J. F.; Li, W. X.; Li, J. J.; Gu, C. Z.; Li, Z. Y. 3D conductive coupling for efficient generation of prominent Fano resonances in metamaterials. *Sci. Rep.* **2016**, *6*, 27817.
[44] Ebbesen, T. W.; Lezec, H. J.; Ghaemi, H. F.; Thio, T.; Wolff, P. A. Extraordinary optical transmission through sub-wavelength hole arrays. *Nature* **1998**, *391*, 667–669.
[45] Mayergoyz, I. D.; Lang, G.; Hung, L.; Tkachuk, S.; Krafft, C.; Rabin, O. Plasmon resonance enhancement of magneto-optic effects in garnets. *J. Appl. Phys.* **2010**, *107*, 09A925.
[46] Huang, H.-T.; Chen, P.-J.; Ger, T.-R.; Chi, Y.-J.; Huang, C.-W.; Liao, K.-T.; Lai, J.-Y.; Chen, J.-Y.; Peng, W. -Y.; Zhang, Q. D. et al. Magneto-optical kerr effect enhanced by surface plasmon resonance and its application on biological detection. *IEEE Trans. Magn.* **2014**, *50*, 1001604.
[47] Manera, M. G.; Ferreiro-Vila, E.; Garcia-Martin, J. M.; Garcia-Martin, A.; Rella, R. Enhanced antibody recognition with a magneto-optic surface plasmon resonance (MO-SPR) sensor. *Biosens. Bioelectron.* **2014**, *58*, 114–120.
[48] Fan, F.; Zhong, C. Z.; Zhang, Z. Y.; Li, S. S.; Chang, S. J. Terahertz chiral sensing and magneto-optical enhancement for ferromagnetic nanofluids in the chiral metasurface. *Nanoscale Adv.* **2021**, *3*, 4790–4798.
[49] Chandra, S.; Cozart, J.; Biswas, A.; Lee, S.; Chanda, D. Magnetoplasmons for ultrasensitive label-free biosensing. *ACS Photonics* **2021**, *8*, 1316–1323.
[50] Li, N. X.; Tang, T. T.; Li, J.; Luo, L.; Sun, P.; Yao, J. Q. Highly sensitive sensors of fluid detection based on magneto-optical optical Tamm state. *Sens. Actuator B: Chem.* **2018**, *265*, 644–651.